LA-UR-17-24807 (Accepted Manuscript)

Role of Surface Chemistry on Catalyst/Ionomer Interactions for Transition Metal–Nitrogen–Carbon Electrocatalysts

Artyushkova, Kateryna
Workman, Michael J.
Gonzales, Ivana
Serov, Alexey
Atanassov, Plamen

To be published in: ACS Applied Energy Materials

DOI to publisher's version: 10.1021/acsaem.7b00002

Permalink to record: http://permalink.lanl.gov/object/view?what=info:lanl-repo/lareport/LA-UR-17-24807

Role of Surface Chemistry on Catalyst/Ionomer Interactions for Transition Metal-Nitrogen-Carbon Electrocatalysts

Kateryna Artyushkova*[a], Michael J. Workman[a], Ivana Matanovic[a,b], Michael J. Dzara[c], Chilan Ngo[c], Svitlana Pylypenko[c], Alexey Serov[a] and Plamen Atanassov[a]

[a] Chemical and Biological Engineering, Center for Micro-Engineered Materials, Albuquerque, NM 87131

[b] Los Alamos National Laboratory, Los Alamos, NM 87545, USA

[c] Department of Chemistry, Colorado School of Mines, Golden, CO 80401, United States

Keywords: PGM-free electrocatalyst, catalyst-ionomer interactions, XPS, catalytic layer chemistry, transition metal-nitrogen-carbon

ABSTRACT. The role of the interaction between doped carbon-based materials and ionic conductors is essential in multiple technologies, from fuel cells and energy storage devices to conductive polymer composites. In this paper, we report how the surface chemistry of transition metal-nitrogen-carbon (MNC) electrocatalysts effects catalyst-ionomer interaction and the resulting structure of cathodes. These interactions and resulting cathode structure modification are related to performance in membrane electrode assembly (MEA) fuel cells. Understanding of the structure of electrodes for the oxygen reduction reaction, distribution and chemistry of active sites, and ionomer morphology are necessary to advance the development of Platinum group metal (PGM)-free electrodes. To assess catalyst interaction with an ionomer, density functional theory (DFT) is used to calculate adsorption energies of the ionomer side chain on different nitrogen species. The high surface concentration of hydrogenated and protonated nitrogen in MNC catalysts causes inefficient ionomer morphology, while an abundance of surface oxides promotes efficient distribution of active sites and optimal ionomer-catalyst interface. The critical role of protonation of nitrogen in catalytic layers in inhibiting proton transport during fuel cell operation is also discussed. This is the first report of the effect of the surface chemistry of MNC catalysts, in the presence of the ionomer, on the structure and performance of MEA electrodes.

Introduction

Polymer electrolyte membrane fuel cells (PEMFC) are a promising technology for power generation for stationary and portable applications. Chemistry, morphology, and surface energy of the cathode catalyst layer have the most significant impact on overall fuel cell performance, and on water balance, since water is produced in this layer. The structure of the catalyst layer must be optimized to contain a high density of accessible active sites and to provide efficient transport of electrons & protons, a reactant gas, and liquid water.

Optimization of both Pt-based and Pt group metal-free (PGM-free) oxygen reduction reaction (ORR) PEMFC cathodes depends on the interactions of the catalyst with an ionomer.[1] Ionomer-catalyst interactions control the overall morphological and chemical structure of the catalyst layer, which in turn affects proton transport, oxygen permeability, and ORR kinetics.[2-3]

In recent years, a significant body of research has emerged to focus on studies of specific interactions between perfluorosulfonic acid (PFSA) ionomer and Pt/C agglomerates, in relation to the understanding the catalyst layer structure and its effect on fuel cell performance.[2-5] At the same time, efforts to replace Pt-based electrocatalysts by PGM-free alternatives – particularly transition metal-nitrogen-carbon (MNC) electrocatalysts – have advanced significantly, and highly active and durable materials tested under fuel cell conditions have been reported.[6-20] Significant advances have been made by studies focused on the chemistry of catalysts, and their kinetic performance as determined by RRDE and, recently, by single membrane electrode assembly (MEA) tests [1, 17, 19-20]. However, understanding the structure of catalyst layers, including distribution of active sites and ionomer morphology within cathode catalyst layers is necessary to advance the development of active and stable electrodes based on MNC systems.

A limited number of spectroscopic and microscopic technologies are appropriate for the elucidation of the chemical and physical structure of the catalytic layer, in particular, the distribution of active sites and morphology of ionomer. X-ray Photoelectron Spectroscopy (XPS) is a very powerful analytical tool that has been proven successful not only in distinguishing between types of active sites in MNC, but also in ionomer orientation for Pt-based materials. [21-26]

In this report, we focus on the chemistry of MNC-based catalyst layers determined by XPS and the effect of catalyst and ionomer interactions on performance in full MEA testing. For the first time, we are reporting results of spectroscopic analysis of the catalytic layer, particularly the density of active sites and ionomer/active site interface chemistry, and their relationship to fuel cell performance data for a series of MNC-based electrodes. The chemical composition of catalytic layers that results in the best catalyst-ionomer interface and its relationship to original catalyst chemistry is discovered. Moreover, the inhibiting role of protonated nitrogen in proton transport is discussed.

Experimental Section

Experimental Details. Iron-nicarbazin derived (Fe-NCB) electrocatalysts were prepared by sacrificial support method described in detail by Workman et al.[14] The inks were composed of 2:1 isopropyl alcohol:deionized water (v:v), catalyst, and D2021 Nafion® (measured to a final loading of 45 wt%) dispersion mixed to a ratio of 3.5wt% total solids. Fuel cell testing was performed by Pajarito Powder, LLC. MEAs with an area of 5 cm^2 were prepared from gas diffusion electrodes (GDEs). The details of MEA manufacturing are discussed in the previous report. [14] The MEAs were loaded into the cell testing assembly (Fuel Cell Technologies Inc.) using single serpentine pattern graphite flow plates, and the cell hardware was assembled using 40 inch-lbs torque. Testing parameters were 80 °C, 100% RH, 250 sccm H_2/200 sccm air at the anode and cathode,

respectively, at an absolute pressure of 1.65 atm. The MEA was preconditioned with a potentiostatic hold at 0.3 V for 10 minutes. Data was then collected potentiostatically with 60 seconds potential holds and the current at the end of the hold reported.

XPS spectra were acquired on a Kratos Axis Ultra X-ray photoelectron spectrometer using a monochromatic Al Kα source operating at 300 W, and data analysis and quantification were performed using CasaXPS software. Three regions per samples were analyzed. Survey spectra were acquired at 80 eV pass energy. High-resolution F 1s, S 2p, O 1s, C 1s and N 1s spectra were acquired at 20 eV pass energy. No charge neutralization was necessary. High-resolution spectra were fitted with a 70% Gaussian/30% Lorentzian line shape with fixed full-width half-max and positions established in previous reports for consistency. [14, 27-28] The parameters used are based on guidance for reproducible peak fitting and comparison between a number of fitted spectra specified in ISO 19830:2015. [29] The average composition and speciation from three areas and standard deviations are included in all structure-to-property plots.

Scanning transmission electron microscope (STEM) imaging and energy dispersive x-ray spectroscopy (EDS) measurements were conducted using an FEI Talos F200X operated at 200 kV. EDS data was acquired and processed using Bruker ESPIRIT software.

Raman spectra were acquired using WITec alpha300 spectrometer. Three areas per sample were obtained.

Computational Details. All the calculations were performed using Density Functional Theory (DFT) with the Perdew-Burke-Ernzerhof (PBE) functional[30-31] and projector augmented-wave pseudopotentials with the use of Vienna Ab initio Software Package (VASP)[32-34]. Extended surfaces containing FeN_4 and graphitic N were modelled using a 4x2 orthorhombic graphene super cell with the dimensions of 9.84 Å x 8.52 Å and a vacuum region of 15 Å. Edge defects with pyrrolic and hydrogenated pyridinic nitrogen were modelled using the nanoribbons, which were constructed from 4x2 orthorhombic super cells with the size of 9.84 Å x 23.52 Å and with a vacuum regions of 15 Å in z- and y-direction [28].The electronic energies were calculated using Gaussian smearing of Fermi level of σ=0.2 eV and gamma centered 8x8x1 k-point grid in the case of the 4x2 orthorhombic super cells and 8x1x1 k-points in the case of the super cells used to model edge defects. In all the cases, plane-wave basis cut off was set to 800 eV. Interaction of different defects with the Nafion side chain was modeled as the interaction between the defect and the representative $CF_3CF_2SO_3$ fragment. [5] Adsorption energies (ΔEad) were calculated using the following formula:

$$\Delta E_{ad} = E_{surface+ad} - [E_{surface} + E_{ad}],$$

where $E_{surface+ad}$ is the energy of the $CF_3CF_2SO_3$ fragment adsorbed on the certain defect, $E_{surafce}$ is the energy of the clean surface/nanoribbon, and E_{ad} is the energy of the $CF_3CF_2SO_3$ fragment in the gas phase. Gas phase studies capture main effects that define the interaction between larger ions and the catalyst surface well as was supported by our previous studies. [35-36] In each case, we considered all possible adsorption orientations, including the interaction with CF groups but the results reported in work, correspond to most preferable adsorption site, which in all cases includes the interaction with the end SO_3^- group.

Results and Discussion

Detailed structural characterization, including XPS and TEM/EDS, of MNC catalysts utilized in current studies, was reported previously.[14] Surface area, as measured by BET, ranges between 550 and 650 m^2/g and does not show any relationship with electrochemical performance reported for these materials. [37] The focus of this study is the understanding the link between the chemistry of the catalysts, its influence on chemistry and morphology of the catalyst layer and resulting fuel cell performance.

For Pt-based materials, the ionomer distribution within the catalyst layer depends on hydrophobicity/hydrophilicity of the catalyst support and direct interactions between Nafion ionomer and Pt/C agglomerates. [2, 4, 38-40] Limited studies of interactions between PFSA ionomers and MNC catalysts have been reported so far. [1, 15, 17].

For MNC systems with atomically dispersed iron coordinated to nitrogen within a porous defected graphene network, the interaction will depend on hydrophobicity/hydrophilicity of the catalyst surface – similarly to Pt-materials. The carbonaceous component (the "backbone") of the catalyst is similar in composition to carbon support in Pt-based electrocatalysts, except nitrogen moieties (C-N species) are present in MNC. Therefore, in the case of MNC, surface energetics depend not only on carbon properties but also on the types of nitrogen species that are present within the carbon network. A graphitic carbon network and a multitude of surface oxides of carbon are also present, as is reflected in the high-resolution C 1s spectrum of a representative electrocatalyst in **Figure 1a**. It is known from Pt-based catalytic layers that the degree of interaction between ionomer and catalyst is significantly affected by the concentration of surface carbon-oxygen groups.[4]

A large variety of nitrogen types is typically present in these materials, as captured well by high-resolution XPS N 1s spectrum for the same catalyst as in Figure 1c. For comparison of spectra among different samples and – more importantly – for identification of changes that occur in the spectra when the catalyst is integrated into a catalyst layer with an ionomer, we have utilized the same parameters for consistent peak fitting as in our previous reports.[14, 27-28, 41] The positions and half-width of all peaks were constrained tightly (with +/- 0.1 eV freedom) and used in fitting the spectra of all catalyst and catalyst inks reported herein. Pyridinic N, nitrogen coordinated to iron N_x-Me, hydrogenated nitrogen (such as pyrrolic N or hydrogenated pyridine), graphitic N, cationic nitrogen which has a positive charge (such as quaternary or protonated nitrogen moieties), and finally nitrous oxides are present in these materials. In our previous work, we studied the relationship between nitrogen and carbon chemistry of the catalyst and MEA performance.[14] We have reported that higher amounts of surface oxides, pyridinic N, and nitrogen coordinated to iron contribute to a better performance in both RRDE and fuel cell tests. [14] There are several types of nitrogen coordinated to metal moieties that can be present – ordered symmetrical Fe-N_4 and distorted Fe-N_x where *x* is smaller than 4.[42] A single peak in the XPS N 1s spectra represents all types of nitrogen coordinated to iron.

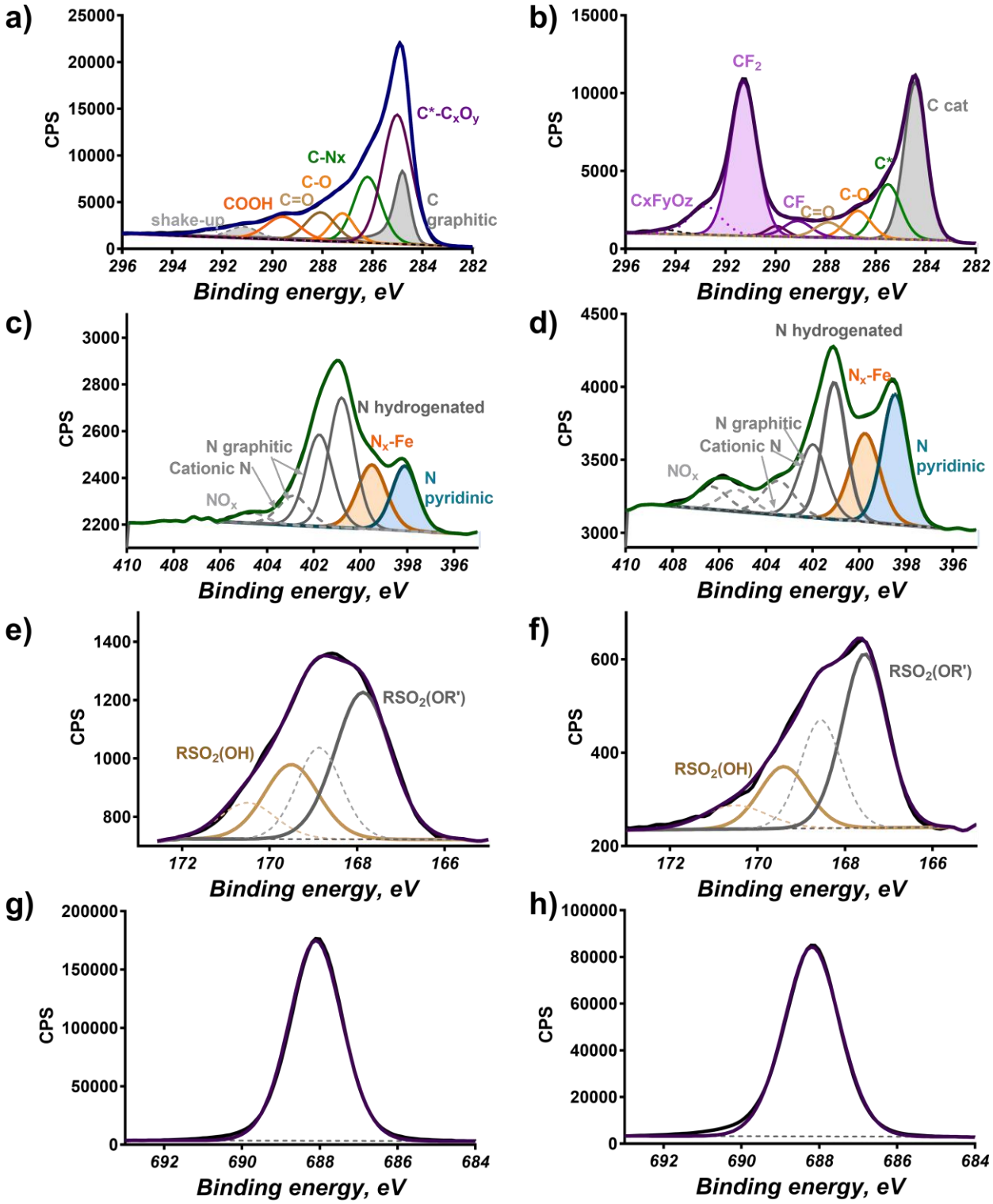

Figure 1. High-resolution XPS spectra for catalyst a) C 1s and c) N 1s; Nafion solvent cast film e) S 2p and d) F 1s; catalyst layer b) C 1s; d) N 1s; f) S 2p and h) F 1s

The ionomer-catalyst interaction is central to understanding the distribution of active sites and morphology of ionomer within the catalytic layer. As discussed above, the most significant difference in the properties of MNC materials in comparison with Pt-based materials in terms of their affinity towards Nafion is the multitude of species present. It is known that surface carbon oxides provide a preferred site for side chain interactions. [43-44] To understand the role of nitrogen species in interactions with an ionomer, we have calculated the adsorption energy of the ionomer side chain with different nitrogen functionalities.

Table 1 shows the DFT-calculated adsorption energies, and **Figure 2** shows optimized geometries of the Fe-N_4 center and hydrogenated pyridine interacting with the side chain ionomer fragment. Theoretical calculations use the chosen fragment as the simplest model capturing the ionomer chemical structure which is commonly used in DFT. [5] The relative strength of interaction between different defects and the ionomer fragment is more important than the absolute values considering limitations between gaseous and aqueous environment. The highest adsorption energy is predicted for nitrogen coordinated to iron, followed by hydrogenated nitrogen such as hydrogenated pyridine or pyrrolic N. Based on DFT calculations and experimental observations of model materials, we reported that the hydrogenated N atoms in a five- or six-membered ring (pyrrolic-N and hydrogenated pyridinic-N) are more sensitive to chemical environment changes in the carbon matrix than the pyridinic-N defect. [28] Graphitic nitrogen also interacts quite strongly with the ionomer side chain. Positively charged cationic (protonated) nitrogen-containing groups are also attractive sites for interactions with the negatively charged sulfonate group of Nafion.

Table 1. Adsorption energy of interactions of various types of nitrogen with an SO_3 group of a Nafion fragment calculated by DFT.

Type of nitrogen	Adsorption energy of ionomer fragment, eV
Pyridinic	-0.90
Fe-N_4	-3.30
Graphitic N	-1.90
Hydrogenated pyridinic	-2.26
Pyrrolic	-2.23

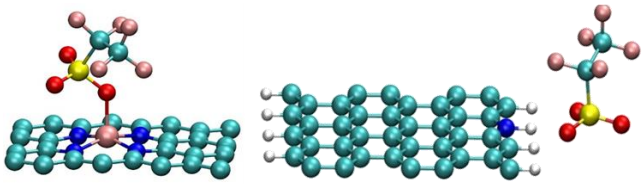

Figure 2. DFT optimized geometries of Fe-N_4 center (left) and hydrogenated pyridine (right) interacting with representative Nafion side chain fragment. Light blue – carbon, blue – nitrogen, pink – iron, red – oxygen, yellow – sulfur, light pink – fluorine.

It is important to note that all the catalysts layers were made utilizing the same weight loading of ionomer and catalyst, so the differences in resulting catalytic activity are only due to differences in chemical composition and structure of resulting catalyst layers. To study the relationship between the chemistry of catalyst layer and MEA activity measured in kinetic (current density at 0.8V), transitional (current density at 0.6 V) and transport (current density at 0.4 V) regimes, we have extracted the surface composition from high-resolution XPS spectra. High-resolution N 1s spectra provide information on the relative distribution of nitrogen species in the catalyst layer, while C 1s spectra provide information on the amount of graphiticity, surface oxide concentration CxOy. Moreover, the ratio of CF_2 to CF extracted from high-resolution C 1s spectra also provides information on ionomer morphology as the ratio of the relative amount Nafion backbone (more of CF_2) to that of the side-chains (more of CF) exposed to the surface.[21] Results with larger CF_2/CF ratio suggest the surface of the catalyst layer that is less hydrophilic, while smaller values suggest a more side chain rich, hydrophilic surface. The difference in the ratio of total fluorine to total sulfur detected also expresses the orientation of ionomer towards the pore with higher F/S ratio detected when backbone is facing the pore. The relative number of active sites facing the surface with respect to the total amount of the ionomer in the catalyst layer can also be obtained from the ratio of the surface concentration of active sites to the surface concentration of fluorine, which is used as a relative measure of ionomer content.

Figures 1b and d show high-resolution C 1s and N 1s spectra obtained from the catalyst layer made using the same catalyst as in Figure 1 a and c. A strong ionomer peak is evident from the high binding energy region of the C 1s spectrum, where C-F, C-F_2, and CxFyOz contribute, as labeled in Figure 1 b. Rearrangement in the shape of the nitrogen spectrum is also apparent. An overall shift to higher binding energy with the larger relative contribution of hydrogenated, graphitic, and cationic (protonated) nitrogen-containing groups is observed in the spectrum from the catalytic layer. DFT calculations support the experimentally observed shift in the nitrogen spectrum in the direction of higher binding energy, which can be attributed to the interaction of the nitrogen species and protonation of nitrogen moieties within the carbon network with the ionomer. Average relative percent of different types of nitrogen species labeled in Figure 1 was calculated from curve-fitted high-resolution N 1s spectra.

In a recent report of the MNC catalyst mixed with Nafion at 1:1 mass ratio, the peak due to pyridinic nitrogen present in the catalyst completely disappeared due to full protonation of pyridine and shifted to a higher binding energy. [45] Due to acidic character of Nafion, protonation of nitrogen in the presence of ionomer is indeed expected, but the intermolecular interactions between nitrogen and sulfonate end groups of the ionomer chain may also contribute to differences in the chemistry of catalytic layers and that of the catalysts themselves as discussed in more details below.

For pure catalysts and catalytic layers tested herein, 20-60% of pyridinic nitrogen present initially in the catalyst was preserved in catalytic layers. The peak due to nitrogen coordinated with iron was retained at 40-90%.

Despite the protonation and interaction of nitrogen species with an ionomer, the densities of active sites within catalytic layers that are directly responsible for ORR plotted in Figure 3 still demonstrate a positive relationship with current densities in the kinetic regime at 0.8 V for MEA fuel cell tests. **Figure 3**a and **3b** plots current densities at 0.8 V versus the relative amount of pyridinic nitrogen and nitrogen coordinated to iron, Nx-M extracted from the fitted high-resolution N 1s spectra. Averages and standard deviations of three areas per samples are plotted for all structure-to-performance plots. The chemical heterogeneity of materials is reflected in the magnitude of standard deviations. Despite high heterogeneity, both pyridinic and nitrogen coordinated with metal preserved in catalytic layers are the active sites with surface concentrations in the electrode contributing to higher ORR kinetics. Current densities in mixed regimes (0.6 and 0.4 V) of polarization curves do not show a strong relationship with a density of these types of nitrogen species (Figure 3c and 3d).

The distribution of active sites with respect to the amount of ionomer present within the catalytic area is studied in **Figure 4a**. Kinetic current densities are related to the ratio of the surface concentration of active sites (total sum of pyridinic nitrogen and nitrogen coordinated to metal obtained from fitting N 1s spectra) to the surface concentration of fluorine, which is used as a relative measure of ionomer content. As this ratio decreases, the current densities decrease significantly due to active sites being blocked by the excess of ionomer.

Another key observation is the relationship between current densities in kinetic and mixed regimes, and surface concentration of cationic nitrogens in catalytic layers (Figure 4b). This group of nitrogen moieties consists of any nitrogen that has a positive charge, such as protonated pyridine, protonated graphitic nitrogen, or quaternary nitrogen. [46] Recently, the study of the effect of protonation of pyridinic nitrogen was linked to worse performance in acidic versus alkaline media, due to a decrease in oxygen affinity to the carbon atoms that are adjacent to protonated nitrogen. [45, 47] The excess amount of cationic-type nitrogen causes a significant decrease in performance due to possible inhibition of available sulfonate groups by extra protons preexisting within the material. Excess protons on the surface of the catalytic layer strongly interact

with side chains of Nafion, thereby decreasing the availability of proton-conducting groups and significantly worsening the effective ion conduction properties of the ionomer.

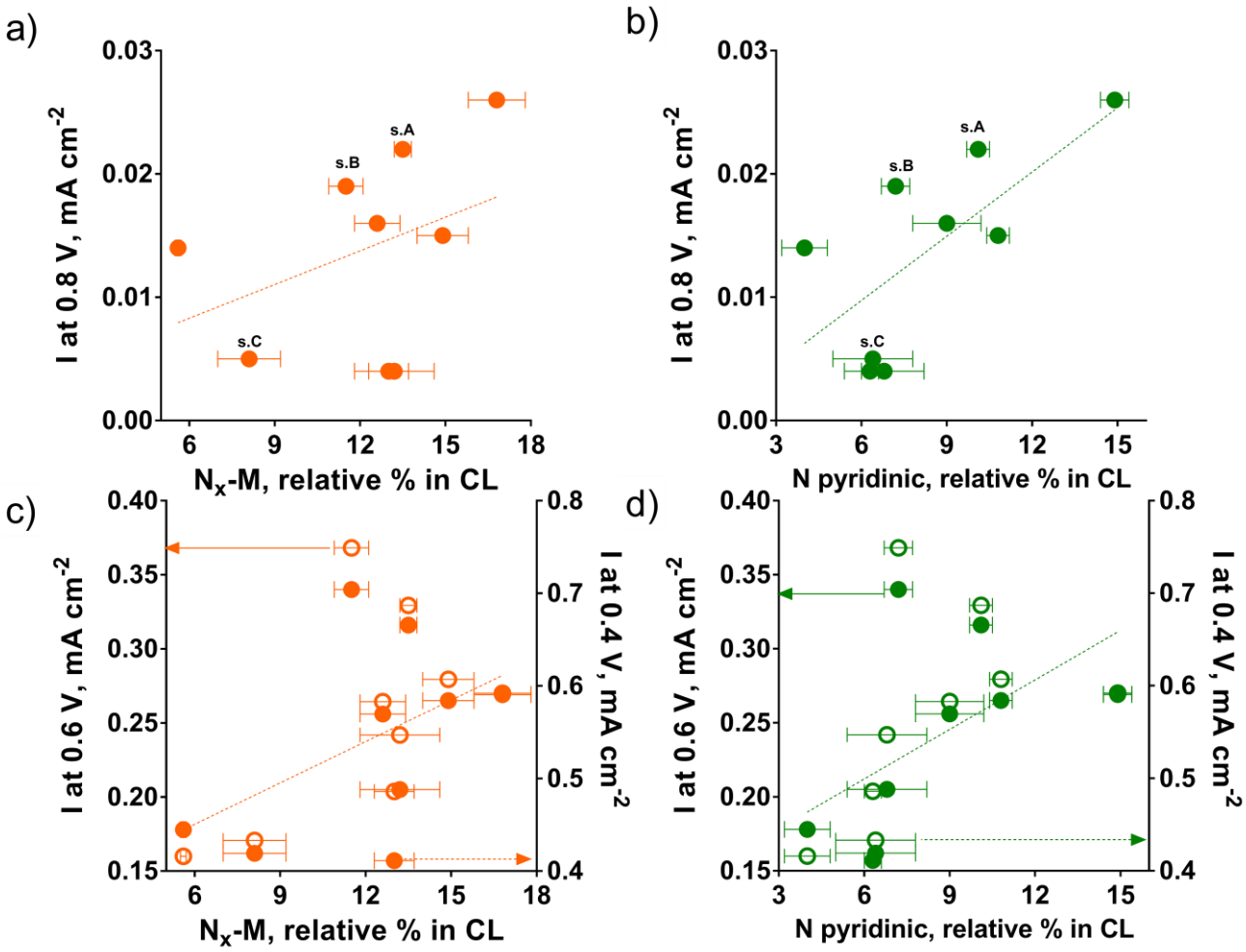

Figure 3. Current density at 0.8 V as a function of a) rel% Nx-M, b) rel % N pyridinic; current density at 0.6 V (solid circles) and 0.4 V (hollow circles) as a function of c) rel% Nx-M, d) rel % N pyridinic.

In our recent studies, the chemistry of catalyst was compared to the chemistry of catalyst exposed to highly acidic buffer solutions. [48] At highly acidic pH=1.1, the percent shift to higher binding energy range expressed as the ratio of the sum of hydrogenated and protonated nitrogen to the sum of pyridinic and Nx-M nitrogen, is on the order of 200%. At lower pH of the acid buffer of 2.4-2.8, this change drops significantly due to the much smaller degree of protonation. For the series of catalysts studied herein, the change in the same ratio is 2-5-fold higher than for highly acidic suspension. Protonation may be a contributing factor to the shift to higher binding energy, but interaction with ionomer is responsible for the much more substantial shift.

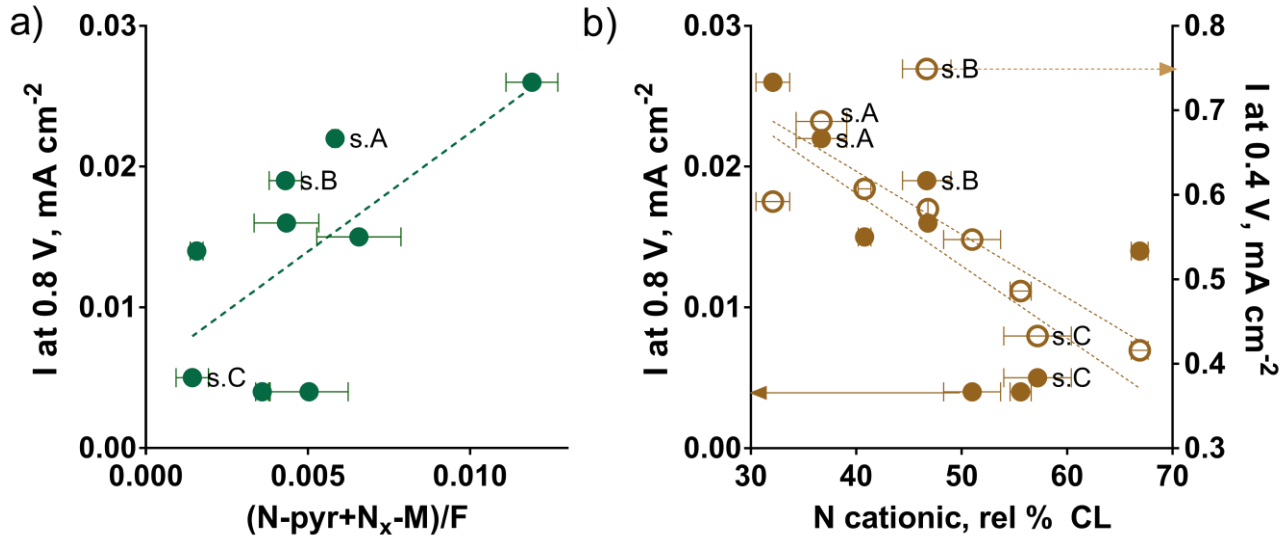

Figure 4. a) current density at 0.8 V as a function of the ratio of catalytically active sites to the total amount of F; b) current density at 0.8 V (solid symbols) and 0.4 V (hollow) as a function of the relative amount of cationic nitrogen.

Raman spectroscopy was performed on three samples that span the range of MEA performance and catalyst-ionomer compositions. The samples are labeled in Figure 5 with sample A being the best performing, sample C being the worst, and sample B being in between. Figure 5 shows representative spectra, while D/G ratios included are averages of three spectra from each catalyst and catalyst ink. For all samples, the D/G ratio increases from the catalyst to the catalyst layer, indicating an increase in the number of defects. The largest change observed is in the worst performing sample #3 for which not only the D/G ratio increases by ~22% but also the width of the peaks increases indicating a very strong change in the catalyst structures upon mixing with an ionomer. For better performing samples, there is a smaller change in D/G ratio upon mixing with an ionomer and no change in shape or width of peaks.

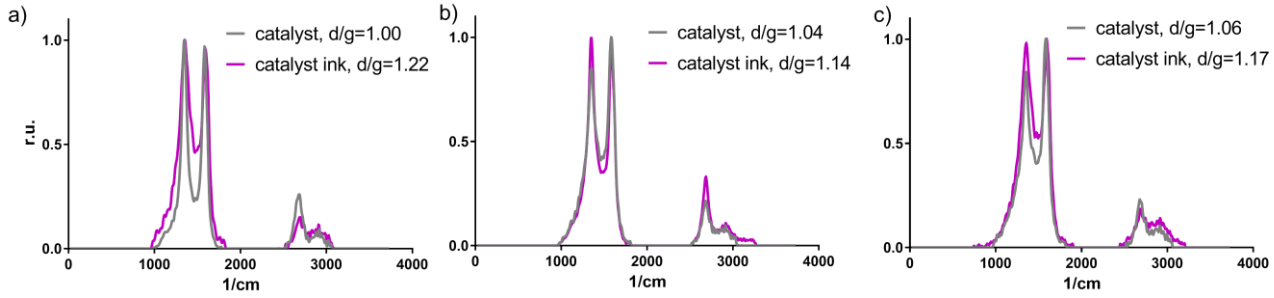

Figure 5. Raman spectra from catalyst and catalyst ink with Nafion for samples A – a, B – b, C – c. Reported D/G ratios are the average of three spectra.

STEM imaging and EDS mapping were used to determine the elemental distribution of catalyst and ionomer within the catalyst layers, for the same three samples Raman is reported on above. While it is important to evaluate catalyst layer morphology at a much smaller scale than the analysis area in XPS, it is equally important to provide quantitative composition of the bulk catalyst layer. The ratios between elements obtained from EDS mapping capture the result of catalyst/ionomer interaction, even though image resolution does not allow direct visualization of nanoscale phenomena.

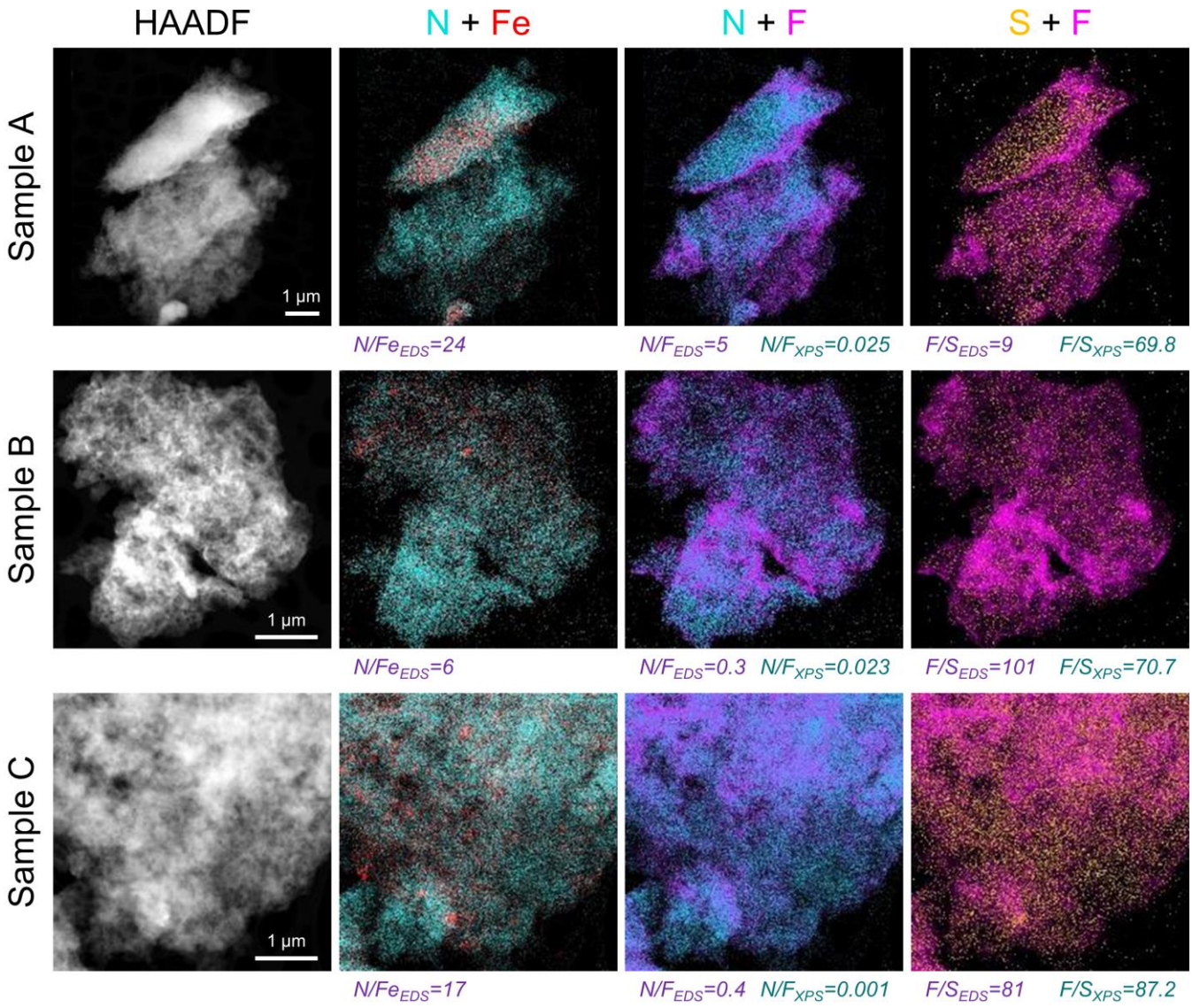

Figure 6. HAADF-STEM imaging and overlays of elemental maps for three samples, with atomic element ratios as-labeled with values obtained from EDS and XPS measurements. Each map pixel corresponds to an EDS spectrum, with visual distribution resulting from assigned colors of blue (nitrogen), red (iron), magenta (fluorine), and yellow (sulfur).

Figure 6 shows high angle annular dark field (HAADF) images and overlay of elemental maps of nitrogen and iron, nitrogen and fluorine, and fluorine and sulfur. Ratios of atomic percentages obtained from quantified EDS data are shown for each sample and compared to the same ratios obtained from XPS. Fe is not detectable in XPS from inks due to attenuation of Fe 2p signal by the fluorine auger peak. The better performing

sample A has larger N/Fe and N/F and smaller F/S ratios. Very different absolute values of ratios of total atomic % of N to that of F obtained from EDS and XPS are due to surface sensitivity of XPS and fluorine segregation on top of the catalyst layer. Both methods show a similar trend with the better performing sample having more nitrogen with respect to total fluorine. The worst performing sample C also has a limited amount of sulfur available. Elemental imaging also shows the distribution of the ionomer with respect to the catalyst, as represented by the nitrogen signal. In the best performing sample, Nafion shows good coverage outside the cluster of the catalyst. In the worst performing sample A, all of the nitrogen is being covered by fluorine, pointing to an excess of ionomer with respect to the catalyst at the surface.

To further evaluate the chemistry and morphology of the ionomer within the catalyst layer, we have used information readily accessible in the F 1s and S 2p XPS spectra. High-resolution spectra of S 2p and F 1s in Figure 1 e) and g) are for Nafion ionomer itself with a single peak in the F 1s spectrum and two peaks in S 2p, identified in reference ionomer films due to coordinated sulfonate $RSO_2(OR')$ at 168 eV and free protonated sulfonic group RSO_3H at higher binding energy of 169.5 eV. There is a small change in S 2p and F 1s upon mixing the Nafion with catalyst (Figure 1 f and h). The peak due to bound sulfonates becomes larger in comparison with the free hydrogenated sulfonic group. The ionomer morphology – and hence, the relative distribution of side chains and backbone facing the pore – result from the interaction of Nafion with the surface species of catalyst via the sulfonate group. Two spectroscopic metrics can be derived from XPS to evaluate the resulting ionomer morphology: 1) ratio of overall fluorine to sulfur peak, F/S, and 2) the ratio of C-F to CF_2 peaks, which are well separated in the C 1s XPS spectrum. For a thick solvent cast film of Nafion®1100 EW, the ratio of CF_2/CF was ~10, which is close to the theoretical ratio of 9. In the thick film, both side chains and backbone are contributing to the overall XPS signal as they are not engaged in any interactions with the substrate. In the thin-film configuration where Nafion is mixed with a catalyst, CF_2/CF ratios of greater than 10 suggest that the pore surface is more backbone-rich and less hydrophilic, while values less than 10 suggest a more side-chain rich, hydrophilic surface of the pore. The higher the degree of interactions of ionomer sulfonate side chain with the surface functional groups of the catalyst, the more backbone will be facing the pore, resulting in higher F/S and CF_2/CF ratios.

Figure 7 plots current densities in kinetic and mixed regimes as a function of the two ratios discussed. As F/S increases from 65 to 90 (Figure 7a), the current densities decrease significantly. EDS mapping shows an even more significant range in bulk F/S ratio (Figure 6). Enrichment of backbone at the surface of the catalyst layers is mainly due to the very strong interaction of sulfonate side-groups with the catalyst surface. Substantial interaction of sulfonate side-groups with the catalyst limits their availability at the pore interfaces, which is essential for efficient proton transport.

The resulting surface of catalyst layers with higher F/S ratio is very hydrophobic, inhibiting water transport as well.

The ratio between CF_2/CF, however, behaves differently. Except for one sample, the trends in Figure 7 c show that the higher ratio corresponds to the higher current densities in both regimes of fuel cell opera-

tion. This indicates that the smaller amount of side chains facing the pore, as manifested by the smaller ratio of CF with respect to CF_2 peak, results in better performance. The trend in F/S ratio indicates that the lack of sulfonate groups is limiting proton transport, while the behavior of the CF_2/CF ratio shows that the excess of exposed side chains results in a hydrophilic catalytic layer surface, which is also detrimental towards performance.

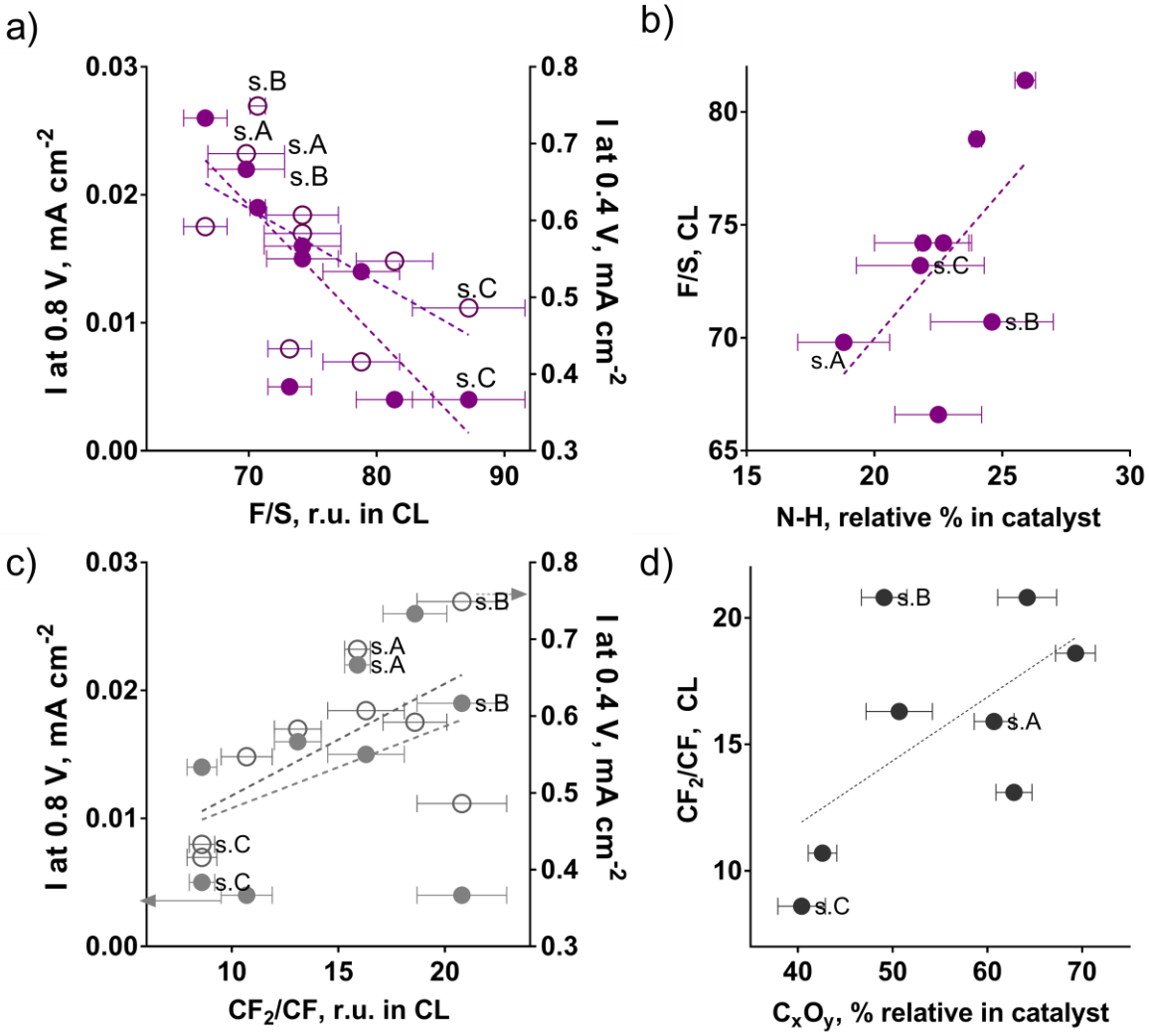

Figure 7. Current density at 0.8 V (solid circles) and at 0.4 V (hollow circles) as a function of a) F/S and c) CF2/CF ratios. F/S ratio as a function hydrogenated N in catalyst b) and CF2/CF ratio as a function of amount of surface oxides in catalysts d)

To produce a good performance, the optimal morphology of the ionomer within the catalyst layer depends on how the ionomer side chains interact with certain carbon and nitrogen groups of the catalyst, which in turn depends on the catalyst properties itself. Based on the DFT discussed above, iron coordinated to nitrogen and hydrogenated nitrogens have the highest affinity towards the side chains of the ionomer. Indeed, as Figure 7b shows, the higher the amount of hydrogenated nitrogens present at the surface of the catalyst, the higher the resulting F/S ratio within the catalytic layer. These trends are due to the complete

engagement of side chains in the interaction with catalyst, limiting the availability of side chains for proton transport at the interface with the pores. At the same time, surface oxide groups on the surface of the catalyst promote a beneficial ratio of CF_2/CF within the catalyst layer (Figure 7d). *Thus, the optimal catalyst chemistry that results in the catalyst layer morphology with sufficient amount of ionomer sulfonate groups for proton transport, but is not too hydrophilic to prevent water flooding, consists of minimum amounts of hydrogenated nitrogens and high amounts of surface oxides.*

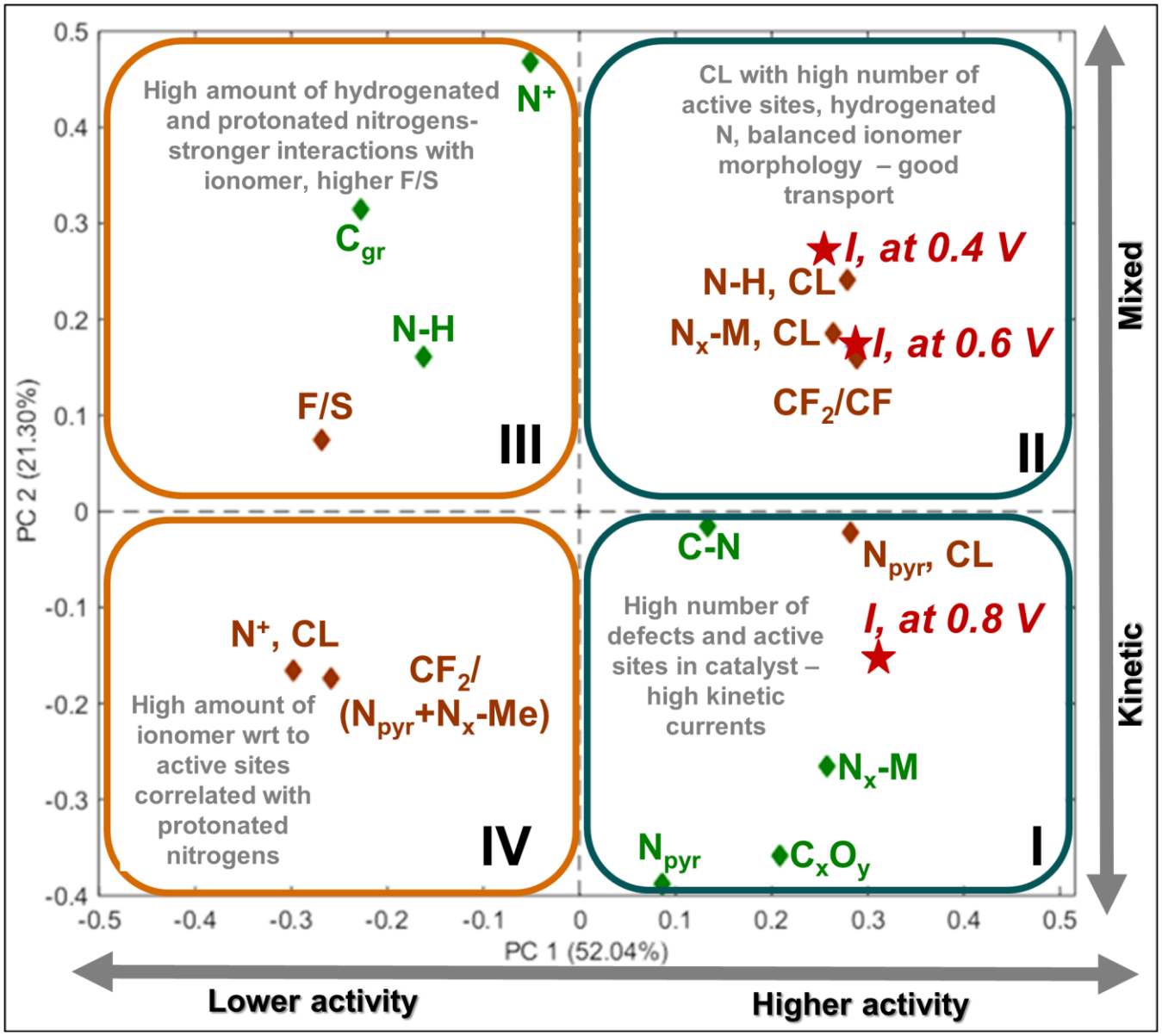

Figure 8. PCA loading plot of data combining surface composition of catalysts, catalyst layers, and current densities at 0.8, 0.6 and 0.4 V

Figure 8 shows a summary of relationships between the chemistry of catalysts, the chemistry of catalytic layers, and the resulting performance, represented by a biplot obtained through the application of Principal Component Analysis (PCA) to the data combining various parameters (surface concentration and current

densities measured) for all samples. Principal component 1 separates samples by low (negative x-axis) and high (positive x-axis) ORR activity. Principal component 2 separates samples with higher currents in kinetic regimes (negative y-axis) and higher currents in transport and mixed regime (positive y-axis). Quadrant I shows that a high amount of defects in the carbon network of catalysts – C-N, C_xO_y, and N_x-M - and a high amount of edge defects manifested by a significant surface concentration of pyridinic nitrogens - correlates with high kinetic currents.

Quadrant II captures active sites and species of the catalytic layers that are representative of preferred ionomer morphology (higher CF_2/CF ratio). Nitrogen coordinated with iron as well as hydrogenated nitrogens contribute to a better performance in the mixed regime. Low kinetic activity (quadrant IV) is linked to the high amount of ionomer present with respect to active site density and high surface concentration of cationic nitrogens in the catalytic layer. Quadrant III shows that catalysts with a high concentration of hydrogenated and cationic nitrogens result in overall high F/S ratio, which is indicative of hydrophobic morphology of catalytic layer resulting in weak activity in the mixed regime.

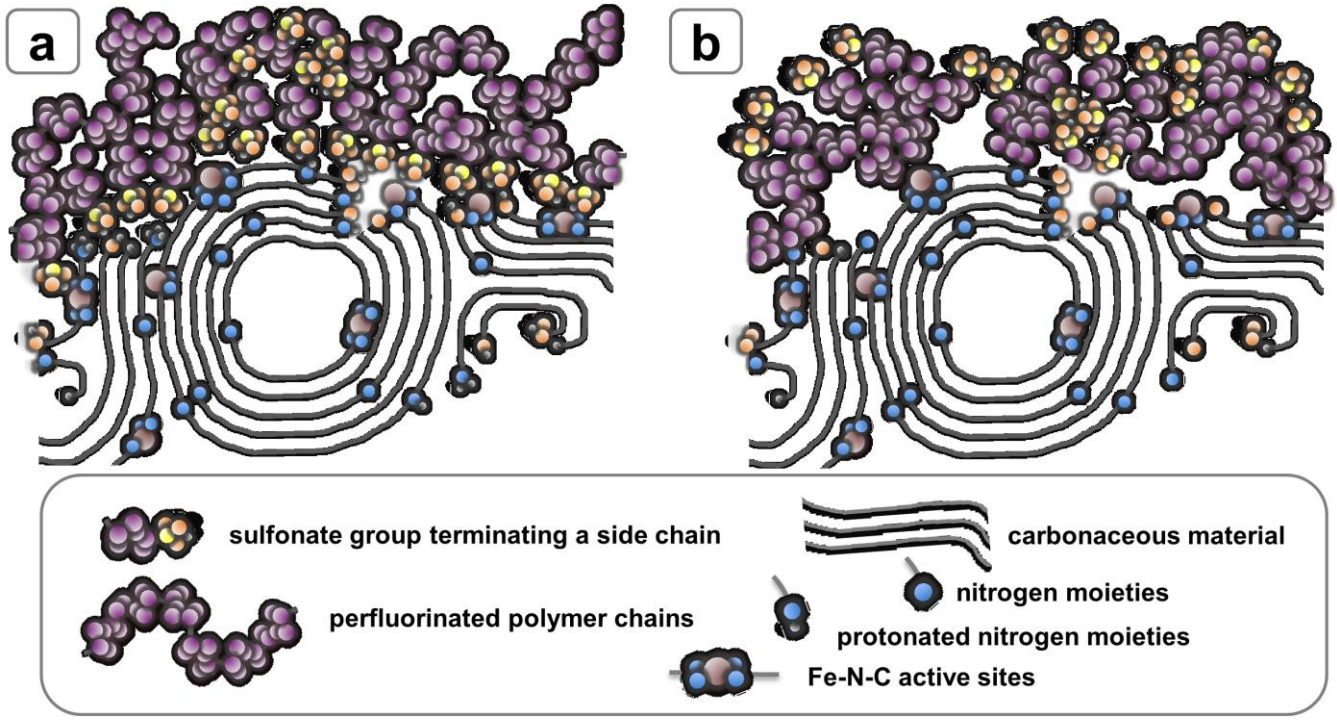

Figure 9. Two types of morphologies of catalyst-ionomer interactions resulting in abundance of sulfonate groups facing the pore (a) and one with a limited amount of sulfonate groups due to their involvement in interactions with the catalyst (b)

From spectroscopic observations of ionomer & catalyst interactions, the resulting catalyst layer chemistry & morphology, and performance in kinetic & transport regimes, we are suggesting two possible extreme cases in morphologies of ionomer and catalyst active sites distribution within the catalytic layer (**Figure 9**). In the first scenario, a catalyst with a minimum number of defects – manifested by small amounts of N_x-M centers, surface carbon oxides, and cationic nitrogen – results in an excess of hydrophilic side chains facing the

pores, potentially causing flooding and blockage of sites accessible for the ORR by the ionomer (Figure 6a). In the second scenario, an excess of the same moieties in the catalyst causes a strong interaction with their side chains, limiting the availability of sulfonate side chains for proton transport and creating water transport limitations due to the overall hydrophobic character of the catalytic layer. Our results point towards significant protonation of surface species within the catalytic layers, which is expected to be amplified during fuel cell operation, contributing to poor proton transport and poor stability.

Conclusion

We report the relationship between the surface chemistry of PGM-free MNC catalysts and the catalyst layer structure that results in the highest electrocatalytic activity for the ORR. Essential information about on the surface composition of the catalyst, as well as the structure and morphology of the catalyst layers derived from XPS is correlated to single MEA performance. Optimal morphology of the PGM-free MNC electrode is obtained when a catalyst contains the smallest amount of hydrogenated and protonated nitrogens and a significant amount of surface oxides. Our results also point towards significant protonation of the surface species within catalytic layers, which is expected to be amplified under fuel cell operating conditions, contributing to the poor proton transport that gives rise to Ohmic losses even at low overpotentials (low current densities).

AUTHOR INFORMATION

Kateryna Artyushkova

Chemical and Biological Engineering, Center for Micro-Engineered Materials, University of New Mexico, Albuquerque, NM, 87131, USA, E-mail: kartyush@unm.edu

Author Contributions

The manuscript was written through contributions of all authors. / All authors have given approval to the final version of the manuscript. /

Funding Sources

NSF GRFP grant #1418062 and Colorado School of Mines start-up funds. Authors also acknowledge graduate student funding through the Betchel fellowship.

ACKNOWLEDGMENT

This work was supported by Center for Micro-Engineered Materials and NSF GRFP grant #1418062. This material is based upon work supported in part by the U. S. Army Research Laboratory and the U. S. Army Research Office under contract/grant number W911NF1410092, “Nanomaterials Characterization Facility: Confocal Raman Microscope/Atomic Force Microscopy - WITec Alpha 300R". VASP license was provided

by the Theoretical Division, LANL, which is supported by the Office of Science of the U.S. Department of Energy under Contract No. DE-AC52-06NA25396. Computational work was performed using the computational resources of EMSL, a national scientific user facility sponsored by the Office of Biological and Environmental Research of the Department of Energy located at Pacific Northwest National Laboratory; NERSC, supported by the Office of Science of the U.S. Department of Energy; and CNMS, sponsored at Oak Ridge National Laboratory by the Scientific User Facilities Division, Office of Basic Energy Sciences, U.S. Department of Energy. This paper has been designated LA-UR XXXXX.

REFERENCES

1. Malko, D.; Lopes, T.; Ticianelli, E. A.; Kucernak, A., A catalyst layer optimisation approach using electrochemical impedance spectroscopy for PEM fuel cells operated with pyrolysed transition metal-N-C catalysts. *Journal of Power Sources* **2016,** *323*, 189-200.
2. Holdcroft, S., Fuel Cell Catalyst Layers: A Polymer Science Perspective. *Chemistry of Materials* **2014,** *26* (1), 381-393.
3. Liu, Y.; Ji, C.; Gu, W.; Baker, D. R.; Jorne, J.; Gasteiger, H. A., Proton Conduction in PEM Fuel Cell Cathodes: Effects of Electrode Thickness and Ionomer Equivalent Weight. *Journal of The Electrochemical Society* **2010,** *157* (8), B1154-B1162.
4. Andersen, S. M., Nano carbon supported platinum catalyst interaction behavior with perfluorosulfonic acid ionomer and their interface structures. *Applied Catalysis B: Environmental* **2016,** *181*, 146-155.
5. Pacheco, R.; Rocco, A. M., Theoretical Description of the Nafion/Platinum Interface by DFT Calculations. *ECS Transactions* **2009,** *25* (1), 1383-1391.
6. Jia, Q.; Ramaswamy, N.; Tylus, U.; Strickland, K.; Li, J.; Serov, A.; Artyushkova, K.; Atanassov, P.; Anibal, J.; Gumeci, C.; Barton, S. C.; Sougrati, M.-T.; Jaouen, F.; Halevi, B.; Mukerjee, S., Spectroscopic insights into the nature of active sites in iron–nitrogen–carbon electrocatalysts for oxygen reduction in acid. *Nano Energy* **2016,** *29* (Supplement C), 65-82.
7. Holby, E. F.; Zelenay, P., Linking structure to function: The search for active sites in non-platinum group metal oxygen reduction reaction catalysts. *Nano Energy* **2016,** *29* (Supplement C), 54-64.
8. Banham, D.; Kishimoto, T.; Sato, T.; Kobayashi, Y.; Narizuka, K.; Ozaki, J.-i.; Zhou, Y.; Marquez, E.; Bai, K.; Ye, S., New insights into non-precious metal catalyst layer designs for proton exchange membrane fuel cells: Improving performance and stability. *Journal of Power Sources* **2017,** *344* (Supplement C), 39-45.
9. Serov, A.; Shum, A. D.; Xiao, X.; De Andrade, V.; Artyushkova, K.; Zenyuk, I. V.; Atanassov, P., Nano-structured platinum group metal-free catalysts and their integration in fuel cell electrode architectures. *Applied Catalysis B: Environmental* **2017**.
10. Ratso, S.; Kruusenberg, I.; Käärik, M.; Kook, M.; Puust, L.; Saar, R.; Leis, J.; Tammeveski, K., Highly efficient transition metal and nitrogen co-doped carbide-derived carbon electrocatalysts for anion exchange membrane fuel cells. *Journal of Power Sources* **2017**.
11. Singh, K.; Razmjooei, F.; Yu, J.-S., Active sites and factors influencing them for efficient oxygen reduction reaction in metal-N coordinated pyrolyzed and non-pyrolyzed catalysts: a review. *Journal of Materials Chemistry A* **2017,** *5* (38), 20095-20119.
12. Jin, Z.; Nie, H.; Yang, Z.; Zhang, J.; Liu, Z.; Xu, X.; Huang, S., Metal-free selenium doped carbon nanotube/graphene networks as a synergistically improved cathode catalyst for oxygen reduction reaction. *Nanoscale* **2012,** *4* (20), 6455-6460.

13. Yang, Z.; Yao, Z.; Li, G.; Fang, G.; Nie, H.; Liu, Z.; Zhou, X.; Chen, X. a.; Huang, S., Sulfur-Doped Graphene as an Efficient Metal-free Cathode Catalyst for Oxygen Reduction. *ACS Nano* **2012,** *6* (1), 205-211.
14. Workman, M. J.; Dzara, M.; Ngo, C.; Pylypenko, S.; Serov, A.; McKinney, S.; Gordon, J.; Atanassov, P.; Artyushkova, K., Platinum group metal-free electrocatalysts: Effects of synthesis on structure and performance in proton-exchange membrane fuel cell cathodes. *Journal of Power Sources* **2017,** *348*, 30-39.
15. Strickland, K.; Miner, E.; Jia, Q.; Tylus, U.; Ramaswamy, N.; Liang, W.; Sougrati, M.-T.; Jaouen, F.; Mukerjee, S., Highly active oxygen reduction non-platinum group metal electrocatalyst without direct metal–nitrogen coordination. *Nature Communications* **2015,** *6*, 7343.
16. Charreteur, F.; Ruggeri, S.; Jaouen, F.; Dodelet, J. P., Increasing the activity of Fe/N/C catalysts in PEM fuel cell cathodes using carbon blacks with a high-disordered carbon content. *Electrochimica Acta* **2008,** *53* (23), 6881-6889.
17. Stariha, S.; Artyushkova, K.; Workman, M. J.; Serov, A.; McKinney, S.; Halevi, B.; Atanassov, P., PGM-free Fe-N-C catalysts for oxygen reduction reaction: Catalyst layer design. *Journal of Power Sources* **2016,** *326*, 43-49.
18. Dombrovskis, J. K.; Palmqvist, A. E. C., Recent Progress in Synthesis, Characterization and Evaluation of Non-Precious Metal Catalysts for the Oxygen Reduction Reaction. *Fuel Cells* **2016,** *16* (1), 4-22.
19. Dombrovskis, J. K.; Prestel, C.; Palmqvist, A. E. C., Optimization of fuel cell membrane electrode assemblies for transition metal ion-chelating ordered mesoporous carbon cathode catalysts a. *APL Mater.* **2014,** *2* (12), 121102.
20. Serov, A.; Workman, M. J.; Artyushkova, K.; Atanassov, P.; McCool, G.; McKinney, S.; Romero, H.; Halevi, B.; Stephenson, T., Highly stable precious metal-free cathode catalyst for fuel cell application. *Journal of Power Sources* **2016,** *327*, 557-564.
21. Artyushkova, K.; Atanassov, P.; Dutta, M.; Wessel, S.; Colbow, V., Structural correlations: Design levers for performance and durability of catalyst layers. *Journal of Power Sources* **2015,** *284*, 631-641.
22. Casella, I. G., An electrochemical and XPS study of Ag-Pb binary alloys incorporated in Nafion (R) coatings. *J Appl Electrochem* **2001,** *31* (4), 481-488.
23. Chen, C.; Levitin, G.; Hess, D. W.; Fuller, T. F., XPS investigation of Nafion (R) membrane degradation. *Journal of Power Sources* **2007,** *169* (2), 288-295.
24. Schulze, M.; Lorenz, M.; Wagner, N.; Gulzow, E., XPS analysis of the degradation of Nafion. *Fresen J Anal Chem* **1999,** *365* (1-3), 106-113.
25. Susac, D.; Kono, M.; Wong, K. C.; Mitchell, K. A. R., XPS study of interfaces in a two-layer light-emitting diode made from PPV and Nafion with ionically exchanged Ru(bpy)(3)(2+). *Appl Surf Sci* **2001,** *174* (1), 43-50.
26. Weber, J.; Janda, P.; Kavan, L.; Jegorov, A., Electrochemical, Ir and Xps Study of Nafion Films Prepared from Hexamethylphosphortriamide Solution. *J Electroanal Chem* **1986,** *199* (1), 81-92.
27. Artyushkova, K.; Serov, A.; Rojas-Carbonell, S.; Atanassov, P., Chemistry of Multitudinous Active Sites for Oxygen Reduction Reaction in Transition Metal-Nitrogen-Carbon Electrocatalysts. *The Journal of Physical Chemistry C* **2015,** *119* (46), 25917–25928.
28. Matanovic, I.; Artyushkova, K.; Strand, M. B.; Dzara, M. J.; Pylypenko, S.; Atanassov, P., Core Level Shifts of Hydrogenated Pyridinic and Pyrrolic Nitrogen in the Nitrogen-Containing Graphene-Based Electrocatalysts: In-Plane vs Edge Defects. *The Journal of Physical Chemistry C* **2016,** *120* (51), 29225-29232.
29. Standardization, I. O. f., Surface chemical analysis -- Electron spectroscopies -- Minimum reporting requirements for peak fitting in X-ray photoelectron spectroscopy. 2015.
30. Perdew, J. P.; Burke, K.; Ernzerhof, M., Generalized Gradient Approximation Made Simple [Phys. Rev. Lett. 77, 3865 (1996)]. *Physical Review Letters* **1997,** *78* (7), 1396-1396.

31. Perdew, J. P.; Burke, K.; Ernzerhof, M., Generalized Gradient Approximation Made Simple. *Physical Review Letters* **1996,** *77* (18), 3865-3868.
32. Kresse, G.; Furthmüller, J., Efficient iterative schemes for ab initio total-energy calculations using a plane-wave basis set. *Physical Review B* **1996,** *54* (16), 11169-11186.
33. Kresse, G.; Hafner, J., Ab initio molecular-dynamics simulation of the liquid-metal–amorphous-semiconductor transition in germanium. *Physical Review B* **1994,** *49* (20), 14251-14269.
34. Kresse, G.; Hafner, J., Ab initio molecular dynamics for liquid metals. *Physical Review B* **1993,** *47* (1), 558-561.
35. Chung, H. T.; Choe, Y.-K.; Martinez, U.; Dumont, J. H.; Mohanty, A.; Bae, C.; Matanovic, I.; Kim, Y. S., Effect of Organic Cations on Hydrogen Oxidation Reaction of Carbon Supported Platinum. *Journal of The Electrochemical Society* **2016,** *163* (14), F1503-F1509.
36. Matanovic, I.; Chung, H. T.; Kim, Y. S., Benzene Adsorption: A Significant Inhibitor for the Hydrogen Oxidation Reaction in Alkaline Conditions. *The Journal of Physical Chemistry Letters* **2017,** *8* (19), 4918-4924.
37. Workman, M. J. A Study of Iron-Nitrogen-Carbon Fuel Cell Catalysts: Chemistry − Nanostructure − Performance. University of New Mexico, 2017.
38. *PEM Fuel Cell Electrocatalysts and Catalyst Layers*. Springer-Verlag London: 2008.
39. He, Q.; Suraweera, N. S.; Joy, D. C.; Keffer, D. J., Structure of the Ionomer Film in Catalyst Layers of Proton Exchange Membrane Fuel Cells. *The Journal of Physical Chemistry C* **2013,** *117* (48), 25305-25316.
40. Weber, A. Z.; Kusoglu, A.; Tesfaye, M., Understanding Ionomer in Fuel-Cell Catalyst Layers. *Meeting Abstracts* **2015,** *MA2015-03* (3), 678.
41. Artyushkova, K.; Matanovic, I.; Halevi, B.; Atanassov, P., Oxygen Binding to Active Sites of Fe–N–C ORR Electrocatalysts Observed by Ambient-Pressure XPS. *The Journal of Physical Chemistry C* **2017,** *121* (5), 2836-2843.
42. Kramm, U. I.; Abs-Wurmbach, I.; Herrmann-Geppert, I.; Radnik, J.; Fiechter, S.; Bogdanoff, P., Influence of the Electron-Density of FeN4-Centers Towards the Catalytic Activity of Pyrolyzed FeTMPPCl-Based ORR-Electrocatalysts. *Journal of the Electrochemical Society* **2011,** *158* (1), B69-B78.
43. Xu, F.; Zhang, H.; Ho, D.; Ilavsky, J.; Justics, M.; Petrache, H.; Stanciu, L.; Xie, J., Investigation of the Interaction of Nafion Ionomer and Carbon Black Using Small Angle X-ray and Small Angle Neutron Scattering. *ECS Transactions* **2011,** *41* (1), 637-645.
44. Yang, F.; Xin, L.; Uzunoglu, A.; Qiu, Y.; Stanciu, L.; Ilavsky, J.; Li, W.; Xie, J., Investigation of the Interaction between Nafion Ionomer and Surface Functionalized Carbon Black Using Both Ultrasmall Angle X-ray Scattering and Cryo-TEM. *ACS Applied Materials & Interfaces* **2017,** *9* (7), 6530-6538.
45. Rauf, M.; Zhao, Y.-D.; Wang, Y.-C.; Zheng, Y.-P.; Chen, C.; Yang, X.-D.; Zhou, Z.-Y.; Sun, S.-G., Insight into the different ORR catalytic activity of Fe/N/C between acidic and alkaline media: Protonation of pyridinic nitrogen. *Electrochemistry Communications* **2016,** *73*, 71-74.
46. Bulusheva, L. G.; Fedorovskaya, E. O.; Kurenya, A. G.; Okotrub, A. V., Supercapacitor performance of nitrogen-doped carbon nanotube arrays. *physica status solidi (b)* **2013,** *250* (12), 2586-2591.
47. Karthikayini, M. P.; Wang, G.; Bhobe, P. A.; Sheelam, A.; Ramani, V. K.; Priolkar, K. R.; Raman, R. K., Effect of Protonated Amine Molecules on the Oxygen Reduction Reaction on Metal-Nitrogen-Carbon-Based Catalysts. *Electrocatalysis* **2016**, 1-12.
48. Rojas-Carbonell, S.; Artyushkova, K.; Serov, A.; Santoro, C.; Matanovic, I.; Atanassov, P., Effect of pH on the Activity of Platinum Group Metal-free Catalysts in Oxygen Reduction Reaction. *ACS Catalysis* **under review**.

TOC